# 1B.5 TURBULENT FLOW OVER AND AROUND SINUSOIDAL BUMPS, HILLS, GAPS AND CRATERS DERIVED FROM LARGE EDDY SIMULATIONS

Peter P. Sullivan[1]*, Edward G. Patton[1] and Keith W. Ayotte[2]

[1]National Center for Atmospheric Research, Boulder, CO
[2]Windlab Systems, Canberra, AU

## 1. INTRODUCTION

A wide spectrum of atmospheric motions impacts the flow environment in and around wind farms. The important time and space scales span an enormous range, large-scale long-time decadal climate down to rapidly evolving thin boundary layers that grow on an individual turbine blade (Schreck et al., 2008). In this scale hierarchy, the atmospheric planetary boundary layer (PBL), where the important scales range from $O$(m) or less to $O$(km) or more, plays a critical if not dominant role in setting the performance of an individual turbine as well as the power output of an entire wind park. PBL motions are turbulent (three-dimensional and time dependent) and couple to larger-scale atmospheric motions and land use, *e.g.,* weather events diurnal heating and cooling, thermal stratification, surface roughness, vegetative canopies, wind waves and local orography all influence wind turbine performance to varying degrees. For example, the afternoon collapse of the heated daytime PBL over the Great Plains followed by surface cooling can lead to a windy weakly stratified boundary layer with a nocturnal jet positioned near hub height $z \sim 100$ m (Beare et al., 2006; Banta et al., 2008). Turbulence in this regime is episodic, non-Gaussian, and can interact with gravity waves and trigger Kelvin-Helmholtz instabilities leading to intermittent loads that fatigue turbine components (Kelley et al., 2003).

The objective of the present work is to describe our recent developments in constructing and utilizing a large-eddy simulation (LES) model for the atmospheric PBL where the lower boundary shape is modestly complex, *i.e.,* we define modestly complex as orography of height $h$ to be a single valued function of the horizontal coordinates $h = h(x, y)$. This enhanced simulation capability will allow us to examine basic interactions between stratified PBL turbulence and landscape features, but also provide information about the winds turbines might be exposed to in a local undulating environment. Understanding the flow environment created by complex small-

*corresponding author address: Peter P. Sullivan, National Center for Atmospheric Research, P. O. Box 3000, Boulder, CO 80307-3000; *email*: pps@ucar.edu

Figure 1: Cathedral Rocks wind farm located above an escarpment on the Eyre Peninsula South Australia adapted from http://www.yorkcivil.com.au/projects/projects/49/cathedral_rocks_wind_farm.

scale topography, as in figure 1, is of particular importance because steep slopes often generate high levels of turbulence in zones of intermittent flow separation. Coupled with background PBL turbulence this orographically generated turbulence can significantly restrict the area available for turbine placement, in which the flow conforms to turbine design standards (IEC, 2005; Ayotte, 2008). We emphasize that a complete simulation of all the turbulence length and time scales generated by the terrain in figure 1 far exceeds current computational capabilities.

## 2. LES ALGORITHM WITH SURFACE TERRAIN

### *2.1 LES with a flat lower boundary*

Typical LES model equations for a dry Boussinesq PBL include at a minimum: a) transport equations for momentum $\rho\overline{\mathbf{u}}$; b) a transport equation for a conserved buoyancy variable (*e.g.,* virtual potential temperature $\overline{\theta}$); c) a discrete Poisson equation for a pressure variable $\Pi$ to enforce incompressibility; and closure expressions for subgrid-scale (SGS) variables, *e.g.,* a subgrid-scale equation for turbulent kinetic energy $e$. Our notation denotes a resolved scale variable by an overbar $\overline{(\ )}$ and thus $\overline{\mathbf{u}}$ are spatially filtered Cartesian velocity components. In our LES code with a flat boundary the spatial discretization is second-order finite difference in the vertical $z$ direction and pseudospectral in horizontal $x-y$ planes. Thus a staggered arrangement of variables is used with $(\overline{u}, \overline{v}, \Pi, \overline{\theta})$ stored at cell centers and $(\overline{w}, e)$ located at cell faces; this variable layout is advantageous because it tightly couples velocity and pressure in our incompressible formulation. The equations are integrated forward in time using a fractional step method utilizing dynamic time stepping with a fixed Courant-Fredrichs-Lewy (CFL) number (Sullivan et al., 1996; Spalart et al., 1991). The code parallelization is accomplished using the Message Passing Interface (MPI) and a 2D domain decomposition. Simulations have used as many as 16,384 computational cores for meshes with $3072^3$ gridpoints (Sullivan and Patton, 2010).

### 2.2 Coordinate transformation

In order to adapt the LES model with a flat lower bottom, outlined in Section 2.1, to an atmospheric PBL flow with a varying boundary shape we apply a conventional grid transformation to the LES equations. The transformation maps the surface following non-orthogonal mesh onto a flat computational space $\boldsymbol{x} \Rightarrow \boldsymbol{\xi}$ according to the rule:

$$
\begin{aligned}
x &= x(\xi) = \xi && \text{(1a)}\\
y &= y(\eta) = \eta && \text{(1b)}\\
z &= z(\xi, \eta, \zeta)\,. && \text{(1c)}
\end{aligned}
$$

The Jacobian, which is needed to move between physical and computational spaces, is (Anderson et al., 1984, see Eq. 5-234)

$$
J = \det \begin{vmatrix} \xi_x & 0 & 0 \\ 0 & \eta_y & 0 \\ \zeta_x & \zeta_y & \zeta_z \end{vmatrix} = \xi_x \eta_y \zeta_z = \zeta_z\,. \qquad (2)
$$

Several strategies are available for building the computational mesh in physical space. Most often we employ simple algebraic stretching (*e.g.,* Anderson et al., 1984, see page 358). This technique builds a smoothly varying mesh along each vertical coordinate line. The stretching factor $K = \triangle z_{k+1}/\triangle z_k$ is the grid spacing ratio between neighboring $k$ and $k+1$ vertical gridpoints. A typical value is $K \sim 1.03$ or less when $\triangle z_1 = 1$ m and the top of the domain is 1000 m and the number of vertical gridpoints $N_z = 256$.

### 2.3 LES equations in curvilinear coordinates

The LES equations in curvilinear coordinates can be derived in a straightforward fashion by applying the chain rule for differentiation. The set of LES equations written in computational coordinates under the transformation (1) and (2) are:

$$
\begin{aligned}
\frac{\partial U_i}{\partial \xi_i} &= 0 && \text{(3a)}\\
\frac{1}{J}\frac{\partial \overline{u}_i}{\partial t} + \frac{\partial}{\partial \xi_j} U_j \overline{u}_i &= \mathcal{F}_i && \text{(3b)}\\
\frac{1}{J}\frac{\partial \overline{\theta}}{\partial t} + \frac{\partial}{\partial \xi_j} U_j \overline{\theta} &= \mathcal{M} && \text{(3c)}\\
\frac{1}{J}\frac{\partial e}{\partial t} + \frac{\partial}{\partial \xi_j} U_j e &= \mathcal{R} && \text{(3d)}\\
\frac{\partial}{\partial \xi_i}\left[\frac{1}{J}\frac{\partial \xi_i}{\partial x_j}\frac{\partial \xi_m}{\partial x_j}\frac{\partial \Pi}{\partial \xi_m}\right] &= \mathcal{S} && \text{(3e)}
\end{aligned}
$$

The equations are expressed in strong conservation form using the "contravariant flux" velocity

$$
U_i = \frac{\overline{u}_j}{J}\frac{\partial \xi_i}{\partial x_j}\,. \qquad (4)
$$

(3a) is the mass conservation (continuity) equation, (3b) is the momentum transport equation, (3c) is the scalar transport equation, (3d) is the subgrid-scale energy transport equation, and (3e) is the pressure Poisson equation. The right hand sides of (3) model physical processes in the atmospheric PBL, *e.g.,* pressure gradients, Coriolis rotation, divergence of subgrid-scale fluxes, buoyancy, and in the case of the SGS $e$ equation also diffusion and dissipation.

A key step in this formulation is co-locating the solution variables $(\overline{\mathbf{u}}, \Pi, \overline{\theta}, e)$ at cell centers (Sullivan et al., 2000, 2008) which leads to a simple compact differencing stencil. In order to maintain tight velocity-pressure coupling the flux velocities $(U, V)$ are located at cell centers while $W$ is located at a cell face. This mimics the variable layout in our usual staggered code with a flat bottom. As in Sullivan et al. (2008) we use momentum interpolation to construct the intermediate right hand sides for the flux velocities. Formally, the equation set (3) has the same structure as in the case with a flat lower boundary and thus similar spatial and temporal discretizations are used to advance them forward in time. Thus the spatial differencing is pseudospectral in the horizontal computational directions $(\xi, \eta)$ and second-order finite differences in the $\zeta$-coordinate.

The major algorithmic change, compared to the flat LES code, is the pressure formulation. As a consequence of the incompressible flow assumption and the non-orthogonal mesh we are forced to solve a general

Poisson equation (3e) for pressure. A direct solution of (3e) is not possible. Inspection of (3a) and (3e) suggests the stationary iteration scheme

$$\mathcal{D}(\Pi^{i+1}) \;=\; \mathcal{D}(\Pi^{i}) \;-\; \frac{1}{\triangle t}\frac{\partial}{\partial \xi_j} U_j(\Pi^{i}) \qquad (5)$$

for $\Pi$ where $\triangle t$ is the timestep the superscript $i$ is an iteration index and the operator $\mathcal{D}$ is an approximate diagonalization of the operator $\mathcal{A}$: $\mathcal{A}$ is the complete left hand side of (3e). At convergence $\mathcal{D}(\Pi^{i}) = \mathcal{D}(\Pi^{i+1})$ and (5) numerically satisfies mass conservation. (5) is designed so that it can be easily inverted using a combination of 2D Fast Fourier Transforms and tridiagonal matrix inversions. Furthermore it nicely maps onto our 2D MPI parallelization.

The algorithm outlined above is a significant advance over our previous scheme (Sullivan et al., 2000, 2008). It uses a more general grid transformation that permits 3D lower boundary shapes, it has a more general and robust pressure solver, and it has an improved treatment of the surface boundary conditions. We have used as many as 4096 computational cores for high resolution simulations, $(1024 \times 384 \times 256)$ gridpoints, with the above scheme. Further details of the algorithm including the posing of the rough wall boundary conditions will be described in a future publication.

## 3. SIMULATION STRATEGY

A series of LES are performed to highlight the interactions between small-scale terrain and PBL turbulence and to exercise the code for both two-dimensional and three-dimensional surface shapes. In these computations, we simplify the external forcing compared to an atmospheric PBL, *i.e.,* we drive the flows with a constant large-scale pressure gradient $\mathcal{P}_x/\rho$ oriented along the $x-$direction and turn off buoyancy influences. Hence the simulations are similar in spirit to a wind tunnel configuration. The lower surface is assumed to be fully rough and we impose $z_o$ boundary conditions based on the winds at the first gridpoint off the surface (*e.g.,* Moeng, 1984).

The simulations with terrain are computationally expensive compared to flat wall LES especially when the slopes of the boundary shape are steep. In these simulations, 20 to 30 iterations of (3e) are required to reduce the residual of the continuity equation (3a) to near machine accuracy. This increases the computational time by a factor of two or more compared to a flat wall simulation. In addition, we use fine mesh resolution $O$(m) (see below) and thus the timesteps are pushed to small values by the CFL constraint in our shear driven computations. Le and Moin (1991) and Zheng and Petzold (2006) propose fractional step schemes that require only a single pressure projection step in their multi-stage Runge-Kutta time stepping schemes which would potentially lower the cost of including terrain in an incompressible LES.

To allow efficient simulations of the various flows described in Section 4.2 we adopt the following strategy: 1) the simulations are first carried forward with a flat bottom until the turbulence is fully developed and the horizontally averaged momentum flux profile is linear in $z$ over the computational domain; 2) we then restart the simulation with the curved lower bottom using a data volume archived at late time from the flat wall case. These simulations are then advanced in time until the turbulence is nearly re-cycled through the computational box. Thus our strategy mimics the conditions in a wind tunnel where a boundary-layer first develops over a flat wall and then encounters an obstacle far downstream of the inlet. This simulation technique is hinted at by Gong et al. (1996, see discussion starting on page 24) and allows both spatial averaging over homogeneous directions (*e.g.,* the $y-$direction) and over a set of realizations. Multiple realizations can be created by simply restarting the terrain simulations using different initial volumes from the flat wall case. The transient induced by inserting the bottom terrain is short lived and not analyzed. The pressure solver is able to generate incompressible flow in a single timestep after inserting the terrain since it is developed from the discrete version of the continuity equation.

## 4. SAMPLE RESULTS

### 4.1 *Turbulent flow past two-dimensional shapes*

Taylor (1998) provides the variation of form (pressure) drag versus waveslope $ak$ for linearized mean flow models with different turbulent closures. The bumps are two-dimensional (no $y$ variation) with shape $h = a\cos 2\pi x/\lambda$: the wavelength $\lambda$ and wavenumber $k$ are related by $\lambda = 2\pi/k$. We re-plot their results in figure 2. At low waveslope, $ak < 0.17$, the theoretical results are nearly independent of the closure. Above $ak > 0.3$ the bumps are steep and the linearized calculations tend to breakdown.

We perform 3D LES of a similar turbulent boundary-layer flow over 2D sinusoidal bumps using a modest grid mesh of $(256, 256, 128)$ gridpoints with a relatively small surface roughness $\lambda/z_o = 5 \times 10^5$. The computations are carried out for four different waveslopes $ak = (0.1, 0.25, 0.35, 0.5)$. At low $ak$ the LES values closely match the linearized calculations. The LES continues to work smoothly for waveslopes as large as 0.5 (this is the largest value tested). An additional LES with a relatively large surface roughness $\lambda/z_o = 1 \times 10^3$ is also shown in figure 2. This value of roughness causes large flow separation with flow reattachment on the forward face of the upstream wave. This is clearly observed in the visualization of the pressure contours and flow vectors. It is interesting that the pressure drag for the small and large roughness are almost identical. We find that in the large roughness case the flow above the bumps tends to skip from crest-to-crest with relatively slow recirculating flow in the wave troughs. In the small roughness (non-separated) case the wave signature is clearly visible in the vertical velocity field but is destroyed by vigorous turbulence generated by flow separation in the large roughness case (see figure 2).

### *4.2 Turbulent flow past three-dimensional shapes*

Hills, ridges, bluffs, land-sea escarpments, *etc.* tend to generate a local speedup in the boundary-layer winds and thus are potential targets for wind turbine sites (see figure 1). Often these orographic features are geometrically complex and 3D, *i.e.,* with their characteristic horizontal lengths and widths of similar scale. Thus it is important to examine the structure of the boundary-layer winds in the presence of 3D obstacles.

We compute turbulent flow over and around three canonical shapes, *viz.,* a hill, gap, and crater. This demonstrates the LES code's ability to handle modestly complex 3D orography and further illustrates the rich level of fluid dynamical phenomenon generated by the interactions between boundary-layer turbulence and small-scale landscape features. In the following sections, the boundary-layer flows are created using the strategy described in Section 3. The simulation with a flat wall is first run for about 130,000 timesteps which is $\sim 7$ large eddy turnover times. Each simulation uses a unique lower-bottom shape and generates a terrain following grid using smooth vertical grid stretching. The computational box $(L_x, L_y, L_z) = (2560, 640, 1000)$ m the number of gridpoints in the three coordinate directions $(N_x, N_y, N_z) = (1024, 256, 256)$ and the horizontal spacing $(\triangle x, \triangle y) = (2.5, 2.5)$ m. The vertical spacing is 1 m at the surface and smoothly increases to the top of the box. Approximately 40 gridpoints are located in the first 50 m above the surface. The large-scale pressure gradient is set to $\mathcal{P}_x/\rho = 1.63\,10^{-4}$ m s$^{-2}$ which generates winds of about 10.5 m s$^{-1}$ at the top of the box. The surface roughness $z_o = 0.05$ m. The flow blockage is small since $h/L_z < 0.05$ everywhere.

#### *4.2.1 Isolated hill*

An isolated 3D hill (see figure 3) is positioned in the simulation with its summit located at $(x_c, y_c) = (1280, 320)$ m. Geometrical properties of the cosine shaped hill are: summit height of 50 m, maximum slope of 0.6, characteristic length scale $\mathcal{L} = 67$ m, and the maximum $x-y$ planform is approximately a circle of diameter equal to $4\mathcal{L} = 268$ m. The shape of the hill is

$$h(x', y') = \frac{b}{2}\left(1 + \cos\frac{2\pi x'}{4\mathcal{L}}\right)\left(1 + \cos\frac{2\pi y'}{4\mathcal{L}}\right) \qquad (6)$$

where $b = 25$ m, $\mathbf{x}' = \mathbf{x} - \mathbf{x}_c$, and $(|x'|, |y'|) < 2\mathcal{L}$.

Figure 3 shows an instantaneous snapshot of typical flow features that develop around the steep isolated hill. The overall impression is that these flow patterns are unique compared to a 2D case with similar characteristic length scale $\mathcal{L}$ and maximum slope. First, a complex flow separation pattern is generated – there is flow separation over the hill crest as in the 2D case but separation also occurs along the flanks of the hill. The region of intense low pressure along the hill crest is confined to a distance of about $2.5\mathcal{L}$ in the $y-$direction. Animations show that the spanwise pressure pattern along the line $x' = 0$ is occasionally interrupted by tongues of low pressure that arc around the hill sides in a crescent shape.

The most striking feature of this simulation however is the complex multi-scale wake flow that develops aft of the hill. It is a collection of temporally evolving vortices with their primary axis aligned with $z$. At any time there can be multiple vortices of various scales present but often two larger vortices dominate the wake as shown in figure 3. There is a strong return flow along the line $y' = 0$ separating the two vortices. Notice also that the location of the vortices is well downstream of the hill summit near the boundary where the hill flattens out and blends into the flat surface; this is clearly downwind of the region of maximum hill slope. Note we are using low pressure as a criterion for vortex identification, see Lin et al. (1996) for a comparison of methods. The coherent rotation of the surface velocity vectors is additional evidence that the regions of low pressure are indeed vortical cores. Broadly, the mean flow patterns shown in figure 3 are similar to the early stage of a flow around a barchan sand dune described by Ortiz and Smolarkiewicz (2009), and the flow measurements around an axisymmetric bump reported by Byun and Simpson (2006).

#### *4.2.2 Gap flow*

Flows in gaps separating ridges and hills are a common landscape feature. The ability of the LES to simulate this type of turbulent flow is shown in figure 4. The shape of the terrain is

$$h(x', y') = \begin{cases} \frac{b}{2}\left(1 + \cos\frac{2\pi x'}{4\mathcal{L}}\right) F(y') & : \quad |x'| < 2\mathcal{L} \\ 0 & : \quad |x'| > 2\mathcal{L} \end{cases} \qquad (7)$$

where the spanwise extent and depth of the gap are controlled by the function

$$F(y') = \begin{cases} \frac{1}{2}\left(1 - \cos\frac{2\pi y'}{4\mathcal{L}}\right) & : \quad |y'| < 2\mathcal{L} \\ 1 & : \quad |y'| > 2\mathcal{L} \end{cases} \qquad (8)$$

Figure 4 illustrates the speedup of the $u-$ component of the horizontal wind in a narrow gap. Notice the speedup is largest in the region where the ridge begins to blend into the gap floor, *i.e.,* along the sides of the gap. Visualization of the pressure field shows a similar feature where the low pressure contours are most negative on the slope approaching the valley and then become less negative away from the gap. The pattern is asymmetric in time shifting from side-to-side in the gap. This is slightly surprising since the initial expectation is that the winds along the gap centerline would be highest. The vertical $y-z$ planes illustrate the vigorous flow separation aft of the two ridges.

### *4.2.3 Crater flow*

Boundary-layer flows in and above open and closed basins are of importance for a variety of applications, *e.g.,* diffusion of pollutants. The recent METCRAX field campaign (Whiteman and CoAuthors, 2008) focused on the complex flow patterns generated by stably-stratified flow in a closed basin. In figure 5 we show an example of the LES code's capability to simulate neutrally stratified flow in an idealized closed crater whose shape $h$ is given by the negative of (6). The nominal diameter is $4\mathcal{L} = 400$ m, the depth equals 50 m, and the maximum slope equals 0.39. The crater center $(x_c, y_c) = (1280, 320)$ m.

The instantaneous snapshot of the flowfield in figure 5 shows several interesting and complex features. The negative (low) pressure contours are indicators of small-scale vortices located near the crater. Animations show a rapid evolution of these vortical structures in the crater interior. The high pressure contours are indicators of the fluctuating re-attachment along the crater backwall and the very negative pressure contours around the crater rim are due to flow accelerations around the crater lip. Visualization in $x-z$ planes along the crater centerline show intermittent ejections of fluid into the overlying boundary-layer flow. We mention that strong convergence of surface streamlines, *e.g.,* as observed at $(x, y) = 1350, 250)$ m in figure 5, is often an indicator of 3D flow separation (*e.g.,* Byun and Simpson, 2006). The flow patterns inside the crater are clearly distinct from those generated behind an isolated hill in figure 3.

## 5. SUMMARY

A massively parallel algorithm and code for large-eddy simulation (LES) of atmospheric planetary boundary layers (PBLs) with modestly complex orography is described. Our LES model equations adopt an incompressible Boussinesq flow model with high Reynolds number rough wall boundary conditions along the lower boundary. A co-located variable layout and a conventional coordinate transformation from physical to computational space are used. The grid mesh in physical space is terrain following and non-orthogonal, a more general formulation can be incorporated into the scheme. The key new step compared to a flat wall code is the formulation of the pressure equation and designing an algorithm for the solution of the pressure Poisson equation. The algorithm is sufficiently general to allow simulations of PBLs over a spectrum of time dependent moving water waves (Sullivan et al., 2010). We present several sample calculations of neutrally-stratified turbulent flow, (similar to a wind-tunnel setup) past 2D sinusoidal bumps and 3D obstacles, *viz.,* a hill, gap, and crater. These calculations highlight the importance of flow separation and coupling with background PBL turbulence, and the ability of the algorithm to simulate turbulent flows with an undulating lower boundary.

In the future we plan to implement an algebraic stress closure model for subgrid-scale fluxes and variances (Wyngaard, 2004) and validate the code against the wind-tunnel measurements of Ayotte and Hughes (2004), and Gong et al. (1996), and field observations. Also, PBL simulations will be carried out with unstable and stable stratification. The fine mesh large-eddy simulations described here can be used in two ways: 1) they provide insight about the fundamental interactions between turbulence and terrain which can impact isolated wind turbines and wind parks; and 2) the detailed datasets can be used for building parameterizations of separated flows.

*Acknowledgments:* We thank Jeff Weil for his contributions to this work. P. Sullivan is partially supported by the Office of Naval Research, Physical Oceanography program and by the National Science Foundation through the National Center for Atmospheric Research. E. Patton is supported by the Army Research Office and NCAR. This research used resources of the National Energy Research Scientific Computing Center, which is supported by the Office of Science of the U.S. Department of Energy under Contract No. DE-AC02-05CH11231, NCAR and the Department of Defense High Performance Computing. Any opinions, findings, and conclusions or recommendations expressed in this publication are those of the author(s) and do not necessarily reflect the views of the National Science Foundation.

## REFERENCES


Anderson, D. A., J. C. Tannehill, and R. H. Pletcher, 1984: *Computational Fluid Mechanics and Heat Transfer*, McGraw-Hill, 599 pp.

Ayotte, K. W., 2008: Computational modeling for wind energy assessment, *Journal of Wind Engr. and Industrial Aerodyanmics*, **96**, 1571–1590.

Ayotte, K. W. and D. E. Hughes, 2004: Observations of boundary-layer wind-tunnel flow over isolated ridges of varying steepness and roughness, *Boundary-Layer Meteorol.*, **112**, 525–556.

Banta, R. M., Y. L. Pichugina, N. D. Kelley, B. Jonkman, and W. A. Brewer, 2008: Doppler lidar measurements of the Great Plains low-level jet: Applications to wind energy, in *14th International Symposium for the Advancement of Boundary Layer Remote Sensing*, volume 1 of *IOP Conf. Series: Earth and Environmental Science*, pp. 1–5, IOP Publishing.

Beare, R. J., M. K. Macvean, A. A. M. Holtslag, J. Cuxart, I. Esau, J.-C. Golaz, M. A. Jimenez, M. Khairoutdinov, B. Kosovic, D. Lewellen, T. S. Lund, J. K. Lundquist, A. McCabe, A. F. Moene, Y. Noh, S. Raasch, and P. P. Sullivan, 2006: An intercomparison of large-eddy simulations of the stable boundary layer, *Boundary-Layer Meteorol.*, **118**, 242–272.

Byun, G. and R. L. Simpson, 2006: Structure of three-dimensional separated flow on an axisymmetric bump, *AIAA Journal*, **44, 5**, 999–1008.

Gong, W., P. A. Taylor, and A. Dörnbrack, 1996: Turbulent boundary-layer flow over fixed aerodynamically rough two-dimensional sinusoidal waves, *J. Fluid Mech.*, **312**, 1–37.

IEC, 2005: Wind turbines - Part 1 design requirements, Technical Report IEC 61400-1, third edition, International Electromechanical Commission, Geneva, Switzerland.

Kelley, N., M. Shirazi, M. Buhl, D. Jager, S. Wilde, J. Adams, J. Bianchi, P. Sullivan, and E. Patton, 2003: Lamar low-level jet project interim report, Technical Report NREL/TP-500-34593, National Renewable Energy Laboratory, Golden, CO.

Le, H. and P. Moin, 1991: An improvement of fractional step methods for the incompressible Navier-Stokes equations, *J. Comp. Phys.*, **92**, 369–379.

Lin, C.-L., J. C. McWilliams, C.-H. Moeng, and P. P. Sullivan, 1996: Coherent structures and dynamics in a neutrally stratified planetary boundary layer flow, *Phys. Fluids*, **8**, 2626–2639.

Moeng, C.-H., 1984: A large-eddy simulation model for the study of planetary boundary-layer turbulence, *J. Atmos. Sci.*, **41**, 2052–2062.

Ortiz, P. and P. K. Smolarkiewicz, 2009: Coupling the dynamics of boundary layers and evolutionary dunes, *Physical Review E*, **79, 041307**, 1–11.

Schreck, S., J. Lundquist, and W. Shaw, 2008: U.S. Department of energy workshop report: Research needs for wind resource characterization, Technical Report NREL/TP-500-43521, National Renewable Energy Laboratory, Golden, CO.

Spalart, P. R., R. D. Moser, and M. M. Rogers, 1991: Spectral methods for the Navier-Stokes equations with one infinite and two periodic directions, *J. Comp. Phys.*, **96**, 297.

Sullivan, P. P., J. B. Edson, T. Hristov, and J. C. McWilliams, 2008: Large eddy simulations and observations of atmospheric marine boundary layers above non-equilibrium surface waves, *J. Atmos. Sci.*, **65**, 1225–1245.

Sullivan, P. P., J. C. McWilliams, and T. Hristov, 2010: A large eddy simulation model of high wind marine boundary layers above a spectrum of resolved moving waves, in *19th Amer. Meteorol. Soc. Symp. on Boundary Layer and Turbulence*, Keystone, CO.

Sullivan, P. P., J. C. McWilliams, and C.-H. Moeng, 1996: A grid nesting method for large-eddy simulation of planetary boundary layer flows, *Boundary-Layer Meteorol.*, **80**, 167–202.

—, 2000: Simulation of turbulent flow over idealized water waves, *J. Fluid Mech.*, **404**, 47–85.

Sullivan, P. P. and E. G. Patton, 2010: The effect of mesh resolution on convective boundary-layer statistics and structures generated by large-eddy simulation, *J. Atmos. Sci.*, **submitted**.

Taylor, P. A., 1998: Turbulent boundary-layer flow over low and moderate slope hills, *Journal of Wind Engr. and Industrial Aerodyanmics*, **74-76**, 25–47.

Whiteman, C. D. and CoAuthors, 2008: METRCRAX 2006: Meteorological experiments in Arizona's meteor crater, *Bull. Amer. Meteorol. Soc.*, **89**, 127–150.

Wyngaard, J. C., 2004: Toward numerical modeling in the Terra Incognita, *J. Atmos. Sci.*, **61**, 1816–1826.

Zheng, Z. and L. Petzold, 2006: Runge-Kutta-Chebyshev projection method, *J. Comp. Phys.*, **219**, 976–991.

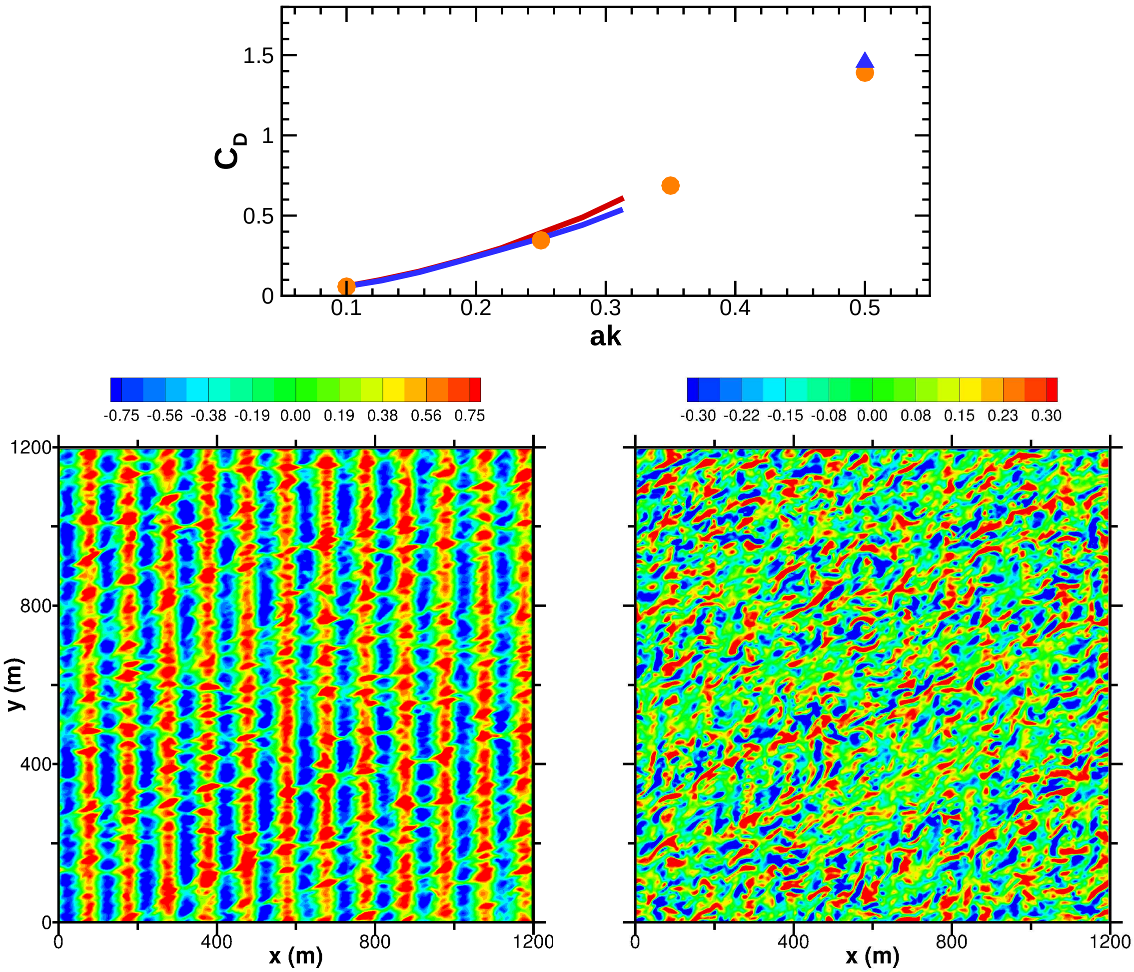


Figure 2: Turbulent flow over 2D sinusoidal bumps. The upper panel shows the pressure drag coefficient $C_D$ as function of waveslope. $C_D$ is obtained from integration of the pressure-waveslope correlation and is normalized by the friction velocity squared $u_*^2$. The lines are theoretical predictions from linearized calculations with different turbulence closures at a small roughness $\lambda/z_o = 10^4$ from Taylor (1998). The orange solid bullets are results from LES with a similar small surface roughness $\lambda/z_o = 5 \times 10^5$. The blue triangle is an LES with large surface roughness $\lambda/z_o = 1 \times 10^3$ which leads to extensive flow separation between the wave crests. The lower panels are visualization of vertical velocity $w$ at a nominal height of $z = 10$ m above the bumps at waveslope $ak = 0.5$ from LES. The left and right panels are small and large roughness $\lambda/z_o = (5 \times 10^5, 1 \times 10^3)$, respectively. The color bar is in units of m s$^{-1}$ and is different between the two plots.

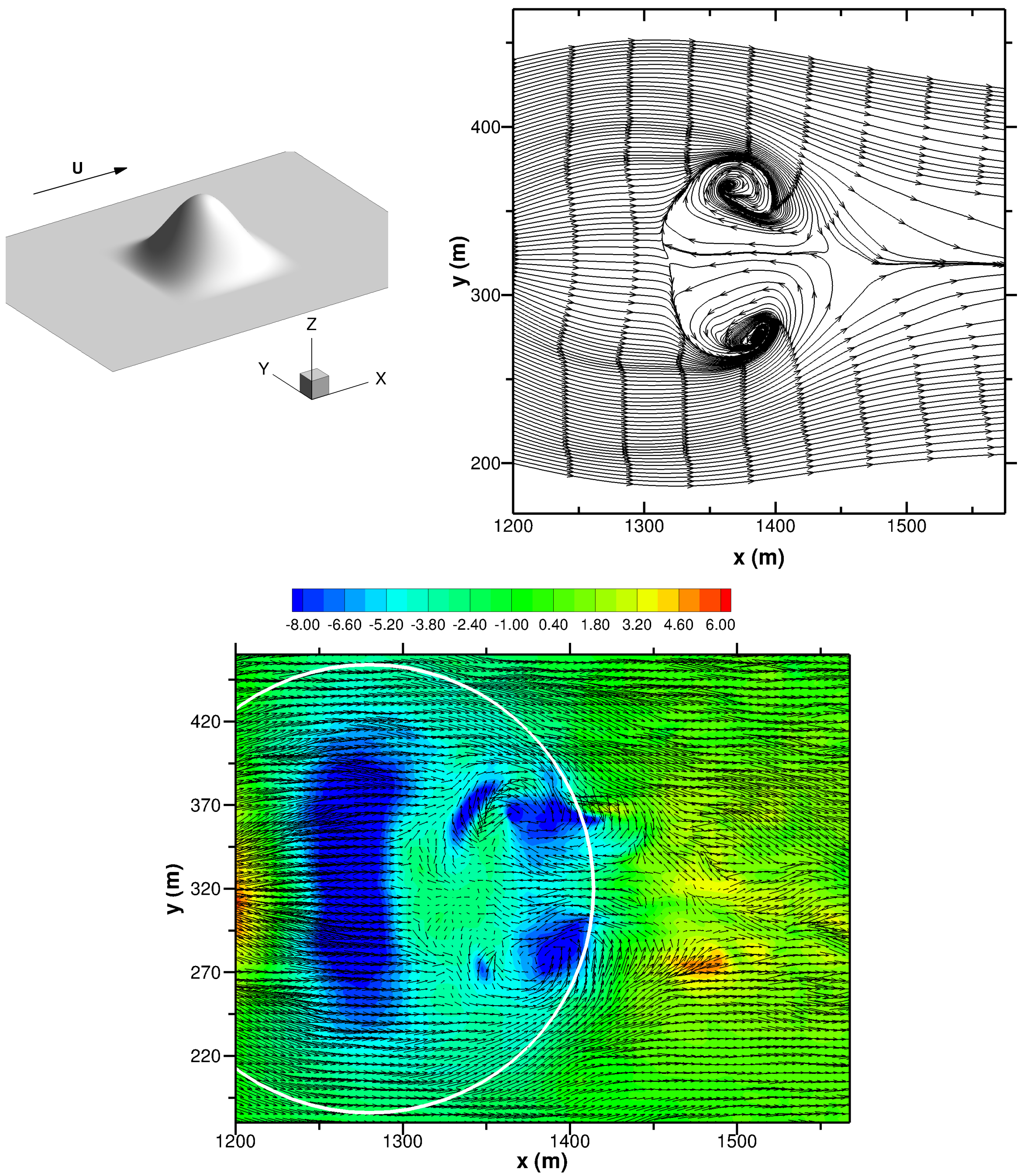


Figure 3: Turbulent flow around a steep 3D hill. The upper left panel shows an oblique view of the hill with the primary flow direction parallel to the $x-$direction. In the upper right panel we show the time averaged streamline patterns around the hill at the height $z = 5.6$ m. In the lower panel we show color contours of fluctuating pressure $p'/\rho$ overlayed with horizontal flow vectors at a nominal height of $z = 5.6$ m above the hill surface. The color bar is in units of m s$^{-2}$. The planform of the hill (*i.e.,* the location where the cosine shaped hill blends into the flat bottom boundary) is approximately indicated by the circular white line. The hill summit $h = 50$ m is located at $(x_c, y_c) = (1280, 320)$ m.

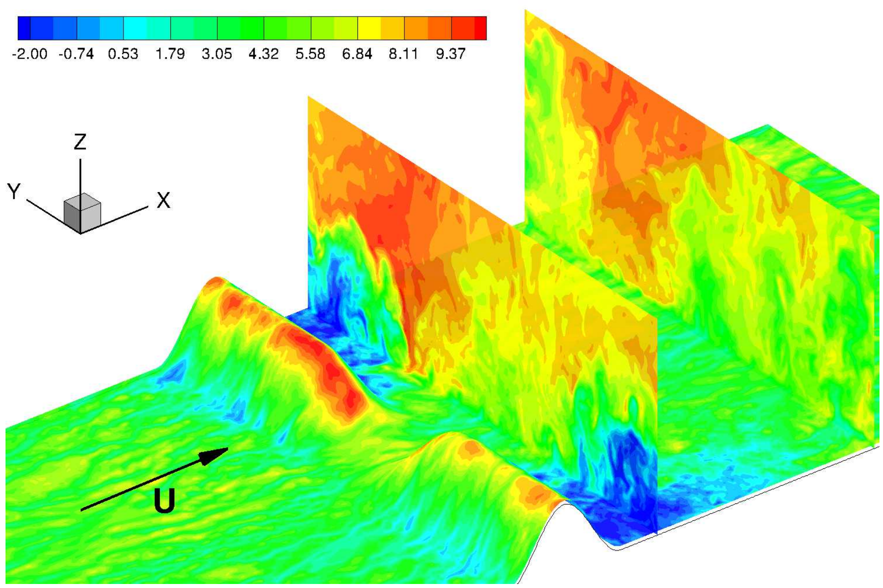


Figure 4: Turbulent flow in a gap between two steep ridges. The primary flow direction is parallel to the $x-$direction. Contours of the instantaneous $u-$velocity component are shown and the color bar is in units of m s$^{-1}$. The two $y-z$ planes are located at $x = (1500, 2000)$ m, and the ridgeline is located at $x = 1280$ m. The horizontal plane is about 4 m off the surface. The lower 150 m of the boundary layer is depicted.

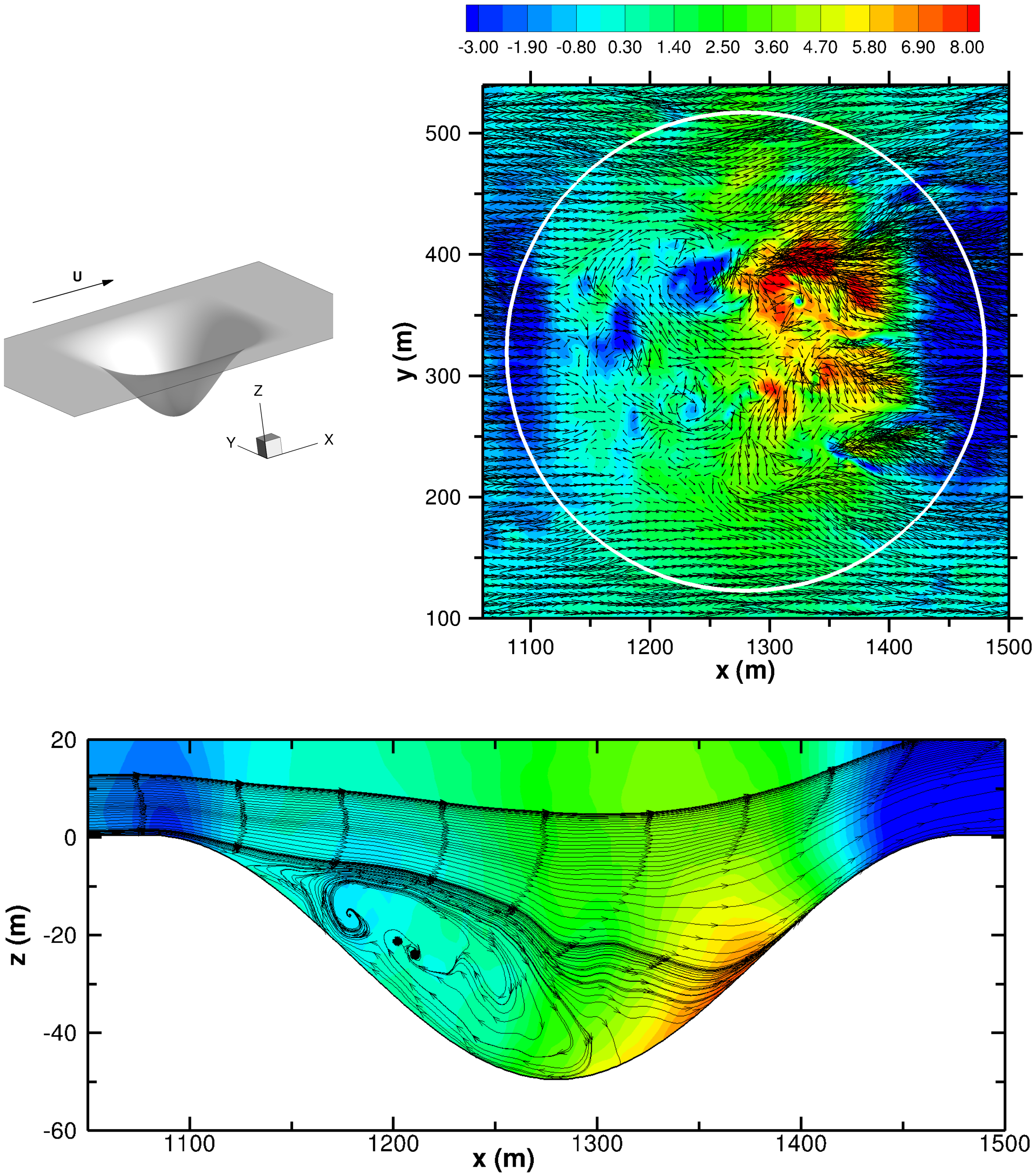


Figure 5: Neutrally stratified turbulent flow in a crater: The upper left panel is an oblique view of the crater geometry. The upper right panel shows instantaneous static pressure contours $p'/\rho$ and horizontal velocity vectors at a nominal height of $z = 2.5$ m above the surface. The white circle is approximately the outline of the crater rim. The color bar is in units of m s$^{-2}$. The bottom panel is a 150 s time average of the streamlines and pressure field in an $x - z$ plane along the crater centerline.